On the Use of X-Band Weather Radar for Wind Field Retrieval in Coastal Zone

Philippe Forget, Marc Saillard, Charles-Antoine Guérin, J. Testud, E. Le Bouar

On the Use of X-Band Weather Radar for Wind Field Retrieval in Coastal Zone

P. FORGET, M. SAILLARD, AND C.-A. GUÉRIN

Mediterranean Institute of Oceanography, Université de Toulon, Université Aix Marseille, CNRS/INSU, IRD, UM110, CS60584, Toulon, France

J. TESTUD AND E. LE BOUAR

NOVIMET, Guyancourt, France

(Manuscript received 10 September 2015, in final form 8 January 2016)

ABSTRACT

This paper documents the study of the radar signature of the sea surface on the images collected by an X-band weather radar and its application to remote sensing of the coastal zone. The main radar parameters considered here are the reflectivity factor [which was converted into a normalized radar cross section (NRCS)], the differential reflectivity, and the mean radial velocity. Measurements of the NRCS in the vicinity of an instrumented offshore buoy allowed for identifying its variations with wind speed and relative direction, which are found to be consistent with the Georgia Institute of Technology (GIT) model and other measurements. A more accurate empirical model for the NRCS is developed. For moderate to strong winds, the mean radial velocity is linearly related to the radial component of the wind speed, showing the potentiality of weather radars to map the radial surface wind speed at the scale of a basin. The influence of surface currents is weak here but should be likely taken into account in other places with stronger currents. Measurements of the differential reflectivity are also consistent with other measurements made elsewhere for the polarization ratio. The analysis of radar data over the entire coverage could also be performed using surface wind estimates from a meteorological model. Similar but less accurate results are obtained for the NRCS and the mean radial velocity. The extra spatial variability not due to wind speed variations is identified. An inversion procedure is proposed to recover the wind vector field from radar measurements after calibration of the NRCS values. Results are promising and pave the way to the concept of weather radar for ocean remote sensing.

1. Introduction

Weather radars are of operational use in national and international weather institutions for quantitative precipitation measurements. The underlying physics and processing techniques have been developed in several textbooks, for example, Doviak and Zrnić (1984), Bringi and Chandrasekar (2001), and Meischner (2004). The performance of a weather radar in terms of coverage (40 000 km^2 typically) and spatial (1000 m) and temporal (5 mn) resolutions allows the continuous monitoring of rainfalls at high resolution over large areas at the scale of countries. Networks of weather radars have been developed world wide since the 1990s. They are now generally equipped with dual-polarized Doppler radars, working at S (10 cm), C (5 cm), or X (3 cm) band. Radar instruments sometimes happen to be close to the coast, with a portion of their coverage at sea up to 100 km offshore, depending on the radar altitude (Fig. 1). Because of a large and increasing demand of in situ data at sea for monitoring and/or modeling purposes, it is appealing to investigate the sea surface signature on weather radar images, if any, and its possible application to coastal oceanography or meteorology. It should be noted that such an opportunistic use of weather radars would require only a small amount of extra investment, as many radar networks are already deployed.

Recent works based on satellite synthetic aperture radar (SAR) data have unveiled the great potential of using the mean Doppler shift over the sea surface for wind field retrieval (e.g., see Mouche et al. 2012 or Dagestad et al. 2013 for a review). As we will show, among other results, this is also the case in the context of coastal weather radars used at grazing incidence, with the advantage of weather

Corresponding author address: Dr. Philippe Forget, MIO, Université de Toulon, CS 60584, 83041 Toulon CEDEX 9, France.
E-mail: forget@univ-tln.fr

DOI: 10.1175/JTECH-D-15-0206.1

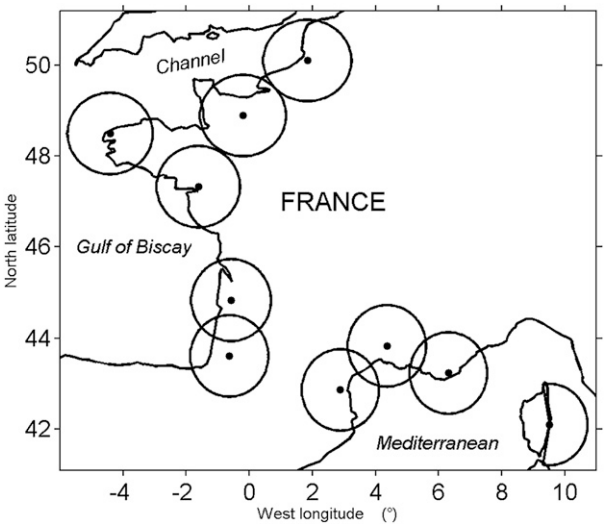

FIG. 1. Weather radars close to the coastline of the French Weather radar network ARAMIS (Météo-France). Radar coverage is shown by the 100-km-radius circles (there is only a circle section on Corsica, southeast).

radars versus SARs to have a much higher temporal coverage.

In the context of sea clutter measurement, weather radars have four important characteristics: they work in the microwave range, at near-grazing angles, with dual polarization, and they collect Doppler information. In this paper the second aspect, although of potential interest, will be only slightly exploited.

The microwave signature of the sea surface in near-grazing conditions is an old but still not completely resolved issue that is still under investigation both experimentally and theoretically. An important motivation is the development of active remote sensing instruments and also the use of microwave radars to measure the properties of short surface waves, which are very difficult to investigate by in situ sensors. The first measurements reported at grazing incidence date back to the end of the 1960s (e.g., Pidgeon 1968). There has been a growing need for physical and empirical models of the mean reflectivity of the sea with respect to radar frequency, grazing angle, sea state, and polarization, with the general purpose of radar performance evaluation (e.g., shipboard radars). One of them, the Georgia Institute of Technology (GIT), is an empirical sea clutter model (Horst et al. 1978) that has received widespread acceptance. An extended dataset by Nathanson (1991) has been used to specify the validity of this model and to develop other reflectivity models (e.g., Gregers-Hansen and Mital 2012). Since the earlier studies on microwave signatures of the sea, specific features have been shown concerning the mean Doppler shift of the sea return, which is often larger for horizontal than for vertical polarization (Pidgeon 1968; Valenzuela and Laing 1970). This feature and other peculiarities of horizontally polarized sea echoes concerning the bandwidth and the polarization ratio have been extensively studied experimentally (e.g., Lee et al. 1995; Rozenberg et al. 1996; Forget et al. 2006) and theoretically (e.g., Wang and Zhang 2011; Miret et al. 2014).

Therefore, weather radar applications can meet observational and operational issues, as well as scientific issues related to the physics of the polarized and coherent microwave signature of the sea at near-grazing incidence.

Retrieving wind (Dankert et al. 2003; Vicen-Bueno et al. 2013) and wave (Young et al. 1985; Vicen-Bueno et al. 2012) information from rotating X-band radars at grazing incidence has been investigated for several years using various processing techniques [e.g., Wave and Surface Current Monitoring System (WAMOS)]. These radars are generally noncoherent. However, coherent radars have also been investigated (Plant et al. 2008; Nwogu and Lyzenga 2010). Weather radars for marine applications can be seen to belong to this class of remote sensing imaging techniques but the spatial scales in range (100 km) and resolution (1 km) differ considerably from other marine radars (5 km and 10 m, respectively) and necessitate ad hoc processing techniques.

This study uses a limited dataset collected by weather radar operating in the south of France for regional monitoring of rain. The radar setup, the principles of data processing for sea clutter parameters estimation, and environmental conditions are described in section 2. Radar data are selected in section 3. Data analysis is done in section 4 in terms of wind and wave parameters at an offshore location where accurate in situ environmental data are available. The analysis is then extended to the entire radar coverage in section 5 using a meteorological model. The analysis includes an attempt of wind field inversion. Conclusions are drawn in section 6.

2. Experiment

a. Radar setup

The Hydrix radar system (http://www.novimet.com/produits/le-radar-hydrix%C2%AE/) was originally designed for atmospheric applications, in particular for precipitation measurements. This instrument has been operating continuously at Mont Vial, north-northwest of Nice, France (Figs. 2, 3), since 2007. An entire month of data records (September 2008) was made available for this study.

The Hydrix radar system is a pulsed, coherent, X-band (9.3 GHz, wavelength $\lambda = 0.0323$ m) scanning polarimetric radar with 2 degrees of freedom in incidence and

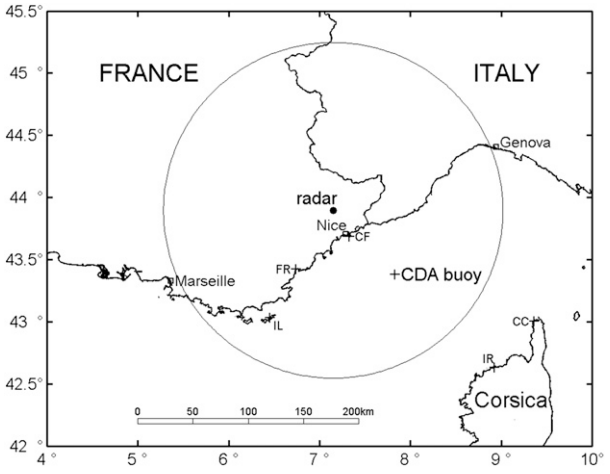

FIG. 2. General geographical conditions. The circle encloses the zone covered by Hydrix and the cone is the zone selected for the present study. IL, FR, CF, IR, and CC designate ground meteorological stations, and CDA is the meteorological buoy.

azimuth. The altitude, h, is 1550 m. The slant range of observation r extends to $r_{\max} = 150$ km along each azimuthal direction. In the geometrical calculations performed in the paper, we will assume that propagation occurs along straight lines over a spherical Earth with an effective radio-electrical radius of $a_E = 8493$ km amounting to four-thirds of the geographical radius of 6370 km. In these conditions, the grazing scattering angle at the sea surface θ_g can be approximated by $\sin^{-1}(h/r - r/2a_E)$ (Long 2001). The value of θ_g obtained using this formula can significantly differ from the flat Earth value $\sin^{-1}(h/r)$, for example, by 40% for $r =$ 100 km. Note that the radio-electrical horizon r_H (162 km here), is slightly higher than the maximum range $r_{\max}$. It is well known that microwave propagation is affected by the vertical changes of the tropospheric refractivity index, which can lead to subrefraction (unstable air) or superrefraction and ducting (due to temperature inversion or evaporation), especially in a littoral environment, where sharp gradients in air temperature and water vapor content can occur (e.g., Sirkova 2011; Haack et al. 2010). This effect results in a modification of the effective Earth radius and then of the values of θ_g.

The elevation angle of the main lobe of the antenna e varies at each rotation. The data used in this study correspond to the lowest elevation angle ($e = -0.4°$), which is the only one showing signatures of the sea surface. A complete azimuthal scan at this elevation angle is achieved in 28 s given the angular speed of the antenna.

The X/R antenna is designed to provide an axisymmetric Gaussian lobe with a 3-dB (one way) beamwidth w of 1.5°, which is modeled by $f(\alpha) = \exp(-4045\alpha^2)$.

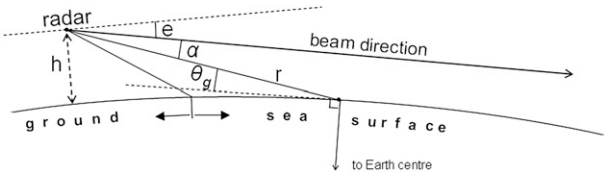

FIG. 3. Radar geometry.

The Gaussian shape of the antenna patterns is expected to hold down to −30 dB from the mean direction. Given the geometrical conditions, this sets a minimum range $r_{\min} = 45$ km beyond which departures from the Gaussian beam can be neglected.

The range resolution is $\delta_r = 300$ m and the angular azimuthal resolution is $\delta_\varphi = 0.5°$, corresponding to an azimuthal width varying from 280 m ($r = 32$ km) to 1309 m ($r = 150$ km). The size of the radar cell at the location of the "Côte d'Azur" (CDA) buoy is 300 m × 707 m. Given the scanning period, δ_φ corresponds to a dwell time of $T_D = 0.0385$ s for each radar bin in range. The Doppler frequency resolution is then $\delta_f = 26$ Hz. The corresponding Doppler spectral bandwidth is half the PRF (500 Hz here), resulting in a number of samples per scan (=PRF × T_D) of 19.

b. Sea clutter parameters

Hydrix provides systematic measurements of the classically employed parameters of precipitation radars (Meischner 2004): the reflectivity factor (Z, mm^6 m^{-3}) in horizontal polarization, the differential reflectivity ($Z_{\rm DR} = Z_{\rm H}/Z_{\rm V}$, where H and V refer to horizontal and vertical polarization, respectively), the differential phase shift (PHI), the correlation coefficient between the H and V signals (RHO), the mean radial velocity (VEL), and the spectral width (SPWI). The algorithm for the extraction of these parameters is described in Le Bouar et al. (2001). Quantities VEL and SPWI together with the backscattered power are computed using the technique known as the pulse-pair processor (Doviak and Zrnić 1984). In this method the moments of the Doppler spectrum are estimated from the autocorrelation function of the temporal signal. We recall the classical radar equation in atmosphere (Skolnik 1980),

$$Z = \frac{512 \log 2 r^2 \lambda^2}{P_t G_M^2 (\delta\theta)^2 \delta_r \pi^3 |K|^2 L_a^2} (P_r + B), \qquad (1)$$

where λ is the radiation wavelength; L_a is the one-way atmospheric attenuation factor; P_t is the transmitted power; G_M is the antenna gain ($=\pi/\delta\theta$ for a Gaussian conical beam); $|K|^2$ is a term depending on the dielectric constant of the scattering particles, which can be assumed constant for water (≈0.93); P_r is the backscattered power;

and B is a background instrumental noise equal to the power recorded in clear air. This equation is routinely used by Hydrix for atmospheric applications. A simple empirical law for L_a is used in the processing of Hydrix data to evaluate the attenuation by atmospheric gazes reading as $10\log(L_a) = -1.0510^{-5}\, r$ (with r in meters). It will be seen further that at the lowest elevation angle of the radar beam and over the sea surface, the contribution from the atmosphere to Z is much smaller than the contribution from the sea. In such cases, P_r coincides with P_{rs}, the power backscattered by the sea surface. The radar equation for a surfacic extended target is (Skolnik 1980)

$$P_{rs} = \frac{P_t G^2(\alpha)\lambda^2}{(4\pi)^3 r^4}\sigma\, dS, \tag{2}$$

where σ is the traditional sea backscattering coefficient (radar cross section per unit area); dS is the radar cell area, equal to $r\delta_r\delta\theta$; and $G^2(\alpha) = G_M^2 f^2(\alpha)$. From Eqs. (1) and (2), we have

$$\sigma_Z = \frac{\pi^6 |K|^2 L_a^2 \delta\theta r}{8\log 2\lambda^4 f^2(\alpha)}(Z - Z_N), \tag{3}$$

where the notation σ_Z is used to avoid confusion with the standard backscattering coefficient. In the following the radar quantity σ_Z is referred to as the normalized radar cross section (NRCS), and Z_N is the noise floor reference and is given in Eq. (1) with $P_r = 0$. In practice, Z_N has been determined from reflectivity images showing no structures over the sea as in Fig. 4a. Several frames have been used and averaged in order to smooth out the small-scale residual noise. It has been verified that Z_N is constant with time.

Contrary to other techniques (e.g., switched dual-polarization configuration), the H- and V-emitted signals in the Hydrix radar system are transmitted simultaneously (e.g., as in Scott et al. 2001). Therefore, Z is proportional to the sum of the received electric signals, $s_{HH} + s_{VH}$, where s_{PQ} refers to the P channel of polarization in emission and Q in reception. For the Hydrix radar system, Q ≡ H and therefore

$$Z = \langle (s_{HH} + s_{VH})(s_{HH} + s_{VH})^* \rangle = \langle |s_{HH}|^2 \rangle + 2\langle s_{HH} s_{VH}^* \rangle + \langle |s_{VH}|^2 \rangle, \tag{4}$$

where the asterisk (*) designates the complex conjugate and the brackets indicate an average over a number of returns from individual radar pulses (practically, 36 pulses are currently used for this estimation. From Eqs. (3) and (4) we have

$$\sigma_Z = \sigma_{HH} + \sigma_{VH} + T_{VH}, \tag{5}$$

where σ_{pq} stands for the different polarization components of the NRCS and T represents the cross term in the right side of Eq. (4). Therefore, the NRCS is a combination of three terms. To evaluate this last term, we use Schwarz's inequality, defined as

$$|\langle s_{HH} s_{VH}^* \rangle|^2 \le \sigma_{HH}\sigma_{VH},$$

which shows that $\sigma_Z = \sigma_{HH}(1 + \varepsilon)$, where $\varepsilon \le R_{VH} + 2R_{VH}^{1/2}$ and $R_{VH}^{(H)} = \sigma_{VH}/\sigma_{HH}$. It follows that $\sigma_Z \approx \sigma_{HH}$ as soon as $R_{VH}^{(H)}$ can be assumed small. It is generally observed that the depolarization of electromagnetic waves by sea surface is negligible at moderate incidence (Valenzuela 1967). The comparison of the respective orders of magnitude of cross and like polarizations is more difficult at grazing angles in view of the weak signal-to-noise ratio and the spiky nature of the time series. There are actually only few such measurements reported in the literature. We will rely on the estimations given by Kalmykov and Pustovoytenko (1976), which show a difference of the order of 10 dB between the like- and cross-polarization signal levels in X band and support $R_{VH}^{(H)} \ll 1$.

In a similar way the pseudo–polarization ratio (PPR) measured by the radar over the sea is given by

$$\mathrm{ZDR} = \frac{\sigma_{HH} + \sigma_{VH} + T_{VH}}{\sigma_{VV} + \sigma_{HV} + T_{HV}}. \tag{6}$$

Here, too, the PPR recovers the classical polarization ratio of horizontal transmit and horizontal receive/vertical transmit and vertical receive (HH/VV) whenever the quantities $R_{VH}^{(H)}$ and $R_{HV}^{(V)}$ ($=\sigma_{HV}/\sigma_{VV}$) remain small.

Last, VEL is also a composite of the velocities of the scatterers that are responsible for HH and HV Doppler signatures. Indeed, according to the pulse-pair technique, VEL is given by

$$\mathrm{VEL} = -\mathrm{PRF}\frac{\lambda}{4\pi}\arg[\langle (s_{HH} + s_{VH})_i (s_{HH} + s_{VH})_{i+1}^* \rangle], \tag{7}$$

where i and $i + 1$ designate two consecutive pulses. As mentioned above the number of pulses currently used for averaging is 36.

In the actual operation conditions of Hydrix (six pulses and about six independent samples), the statistical error in Z is ±2 dB and that in VEL is $\pm 0.25\ \mathrm{m\,s^{-1}}$.

c. Environmental data

Several wind data from Météo-France stations [Ile du Levant (IL), Frejus (FR), Cap Ferrat (CF), Ile Rousse (IR), Cap Corse (CC)] are available in the region (Fig. 2). One of them is of particular interest for the current study, namely, the CDA buoy. It is located 79 km from the radar in the azimuth −46.4° (referred to as the west–east direction) by a water depth of

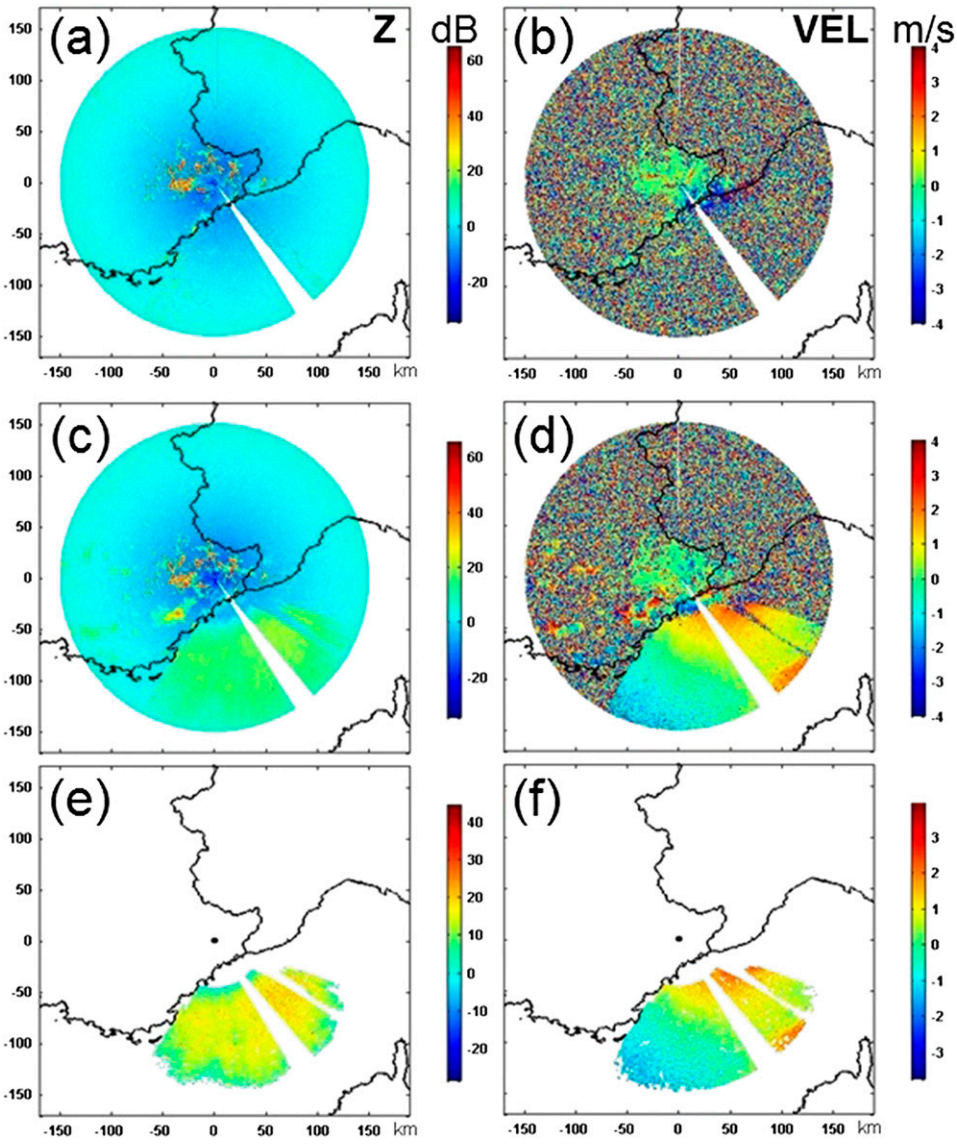

FIG. 4. Images of (left) Z and (right) VEL for (a),(b) low and (c),(d) strong radar backscatter. (e),(f) Images of the sea signatures as selected by specific processing (section 3).

2300 m and a grazing angle $\theta_g = 0.85°$. The buoy carries wind sensors and a Waverider buoy provides wave information (omnidirectional spectrum and wave parameters) at an hourly rate. The wind sensors are located at 3.6 m above the sea surface, and the wind velocity $W_{3.6}$ was converted to the more conventional wind speed at 10-m height, W (subscript 10 is omitted), using Lee et al. (1995) formulas for the vertical wind profile and roughness length–friction velocity relationship. This yields $W = 1.14W_{3.6}$ in a good approximation in the considered range of wind speed (0–15 m s^{-1}). Wind information reported by other meteorological ground stations, although different from those given by the CDA buoy, show the same climatologic variations. The experimental period under consideration corresponds at CDA buoy to winds blowing from northeast and southwest sectors with maximum values of 17 m s^{-1} (Fig. 5). For the present study, a convenient wind statistic concerns dates with valid radar measurements of σ_Z, Z_{DR}, and VEL, and for wind direction, the direction relative to the radar beam axis, θ_{REL} (Table 1). For reasons of symmetry, θ_{REL} was limited to 0°–180° and taken in sectors referred to as downwind (dw), down-crosswind (dcw), crosswind (cw), up-crosswind (ucw), and upwind (uw). The wind statistic obtained is slightly different from the statistics of the full wind record, which gives, for example, values in the last column of the table of 3.2%, 16.3%, 38.2%,

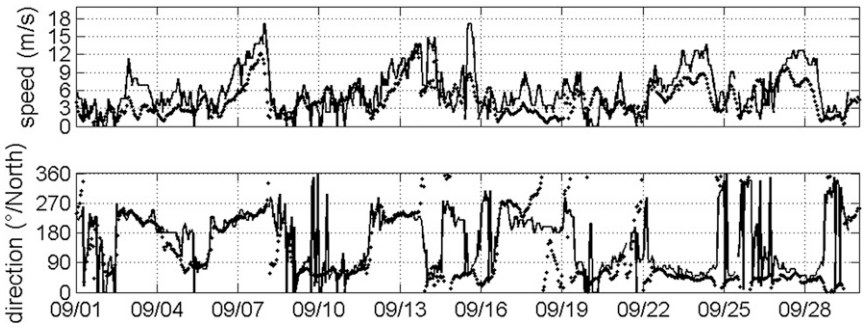

FIG. 5. Wind speed and direction in September 2008 at CDA buoy (lines) and given by MM5 at the same location (dots).

38.8, and 3.6%, respectively. The large majority (90%) of available radar data correspond to cw and ucw.

At the specific dates for which valid radar measurements were available for σ_Z and VEL, the significant wave height (Hs) and the wave period range from 0.4 to 2.7 m and from 2.6 to 9.3 s, respectively. The analysis of the wave spectra has shown that the sea state was dominated in 69% of the cases by wind waves and by swell in the remaining cases. The separation between wind- and swell-dominated wave systems was based on the value of the peak frequency F_p of the wave spectrum as compared to the value predicted by a Pierson–Moskowitz saturated spectrum, $F_p^{(\mathrm{PM})}$, which depends only on W through $F_p^{(\mathrm{PM})} = 1.275W^{-1}$ (Alves et al. 2003). A swell (wind wave)-dominated wave system corresponds to an F_p smaller (greater) than $F_p^{(\mathrm{PM})}$. Certainly, mixed wind sea/swell situations may exist.

In view of the extended radar coverage, we also considered the surface wind data computed by the mesoscale model MM5 operated by ACRI SA Company over the northwestern Mediterranean Sea. MM5, from Pennsylvania State University and the National Center for Atmospheric Research, is embedded in the National Centers for Environmental Prediction weather forecast model and provides 3 h(6 km) time (space) resolutions. In the version we used, model values are interpolated to give a horizontal resolution of 3 km. Time variations of wind direction and velocity from MM5 and from the DCA buoy follow similar trends (Fig. 5). However, if MM5 wind data are in reasonable agreement with the data collected at the CDA buoy for wind direction, discrepancies exist for wind velocity. In particular as seen in Fig. 6 the MM5 wind velocity $W^{(\mathrm{MM5})}$ overestimates W for $W < 3\,\mathrm{m\,s^{-1}}$ and underestimates W at larger velocities. For $W \geq 4\,\mathrm{m\,s^{-1}}$, we obtain on average

$$W^{(\mathrm{MM5})} = 0.65W. \tag{8}$$

Table 2 gives the statistics of MM5 wind at the CDA buoy at the days for which both σ_Z and VEL are available. A comparison of Tables 1 and 2 illustrates the aforementioned differences between model outputs and in situ measurements. For instance, the statistics of the wind direction from the model and from the data are similar, whereas they differ somewhat for wind velocity.

For the discussion about the influence of surface currents on radar measurements, we used a high-resolution circulation model, GLAZUR64, developed by Ourmières et al. (2011) (see also Guihou et al. 2013) and implemented over the northwestern Mediterranean Sea. GLAZUR64 is a configuration of the ocean circulation model Nucleus for European Modelling of the Ocean (NEMO; Madec 2008). The horizontal resolution is 1/64° (about 1.25 km × 1.25 km). There are 130 vertical z levels

TABLE 1. Wind statistics at the CDA buoy for available radar parameters VEL and σ_Z. Values indicate the number of cases corresponding to each class of wind direction and wind velocity. The italics denote the cumulative percentages of cases. Symbols: dw (downwind), dcw (down-crosswind), cw (crosswind), ucw (up-crosswind) and uw (upwind).

Class of wind direction θ_{REL} (°)		Class of wind velocity W ($\mathrm{m\,s^{-1}}$)					
		0–4	4–8	8–12	12–16	16–20	Percent
0.0–22.5	dw	0	2	0	0	0	*0.3*
22.5–67.5	dcw	0	12	6	3	1	*6.0*
67.5–112.5	cw	0	69	64	39	1	*48.7*
112.5–157.5	ucw	15	103	23	5	1	*41.3*
157.5–180.0	uw	5	7	1	0	0	*3.7*
	Percent	*5.6*	*54.1*	*26.3*	*13.2*	*0.8*	

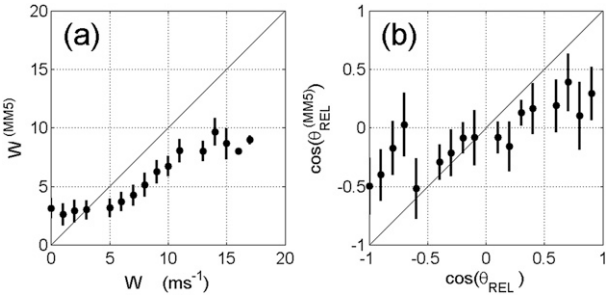

FIG. 6. Comparison of wind parameters measured at CDA buoy and estimated by MM5. (a) Wind velocity and (b) cosine of relative wind direction referred to the radar beam axis passing by the buoy. The length of the vertical bars is equal to the standard deviation of the *y*-axis variable for a given value of the *x*-axis variable.

with a vertical resolution of 1 m for the first 30 m. The data used in this study correspond to the current at 1-m depth averaged over 12 h. The sampling rate is also 12 h.

3. Selection of radar data

In this paper we have decided to consider only the data collected every hour, which is the time scale of variability of meteorological and oceanographic (METOC) conditions. This represents an amount of 720 radar data during September 2008. The small-scale variability in time was investigated on a particular day. Figure 7 is an example of the variation of Z at the nominal sampling rate (150 s) showing the selected hourly data points. The standard deviations of the various signals taken at the hourly rate are 3.0 dB, 2.8 dB, and 0.36 m s^{-1} for Z, Z_{DR}, and VEL, respectively. These values give the order of the accuracy that can be expected for these quantities.

The parameter RHO is known to be a good indicator of the presence of rain (Meischner 2004). It exhibits values exceeding some threshold RHO_{min} when precipitation occurs. This criterion was used to exclude the radar pixels with $RHO > RHO_{min} = 0.80$. An example of rain being present on most of the radar coverage is displayed in Fig. 8.

The relevant observation domain of the radar must be chosen with care before processing and interpretation of the data. First, the radar coverage at sea is the angular sector shown in Fig. 2. Beyond these limits, the signal is significantly attenuated by the shadowing effects from ground obstacles. Second, the narrow blank angular sector pointing to the southeast, which can be seen in the radar images (Figs. 4, 8), is a blind zone due to a masking obstacle in front of the radar. Last, the sea echo seems lost at ranges typically smaller than 50 km, as seen in Figs. 4c,d. This limit is close to the value r_{min} defining the lower range for which the beam can be considered as Gaussian. To summarize we define the effective observation domain as the area delimited by the outer cone and $r > r_{min}$ and excluding the blind zone. The grazing angles in these ranges vary from 1.79° (r_{min}) to 0.09° (r_{max}).

An additional filtering procedure was applied to the radar data. First, we have selected the radar bins having Z values greater than Z_N, the instrumental background level [Eq. (3)]. To minimize the number of isolated pixels, Z_N was augmented by 1.5 dB. A second processing was suggested by the structure of the Doppler velocity fields (VEL). The latter are in general noisy and with no apparent features whenever Z is close to Z_N (Figs. 4a,b). On the contrary, visible spatial structures are present in the case of significant backscatter (Figs. 4c,d). An empirical method was developed to select those radar bins corresponding to such structures. The technique consists of computing the variance of the signal along the bin azimuth and within a window of N neighboring points and rejecting the bin under consideration if this variance is higher than some given threshold VAR_{min}. The choice $VAR_{min} = 1\,m^2\,s^{-2}$ and $N = 8$ was found satisfactory in as much as an image of VEL processed using these parameters was found to exhibit the spatial structures while being free of noise. In a last step, isolated values of Z and velocity fields were discarded. The final Z–VEL images look as in Figs. 4e,f, where the pixels values are expected to carry true geophysical information.

It is interesting to evaluate the part of coverage with valid data for the different quantities Z and VEL, C_Z, and C_{VEL}. This part is defined as the ratio of the number of radar cells with valid measurements to the total number of radar cells within the effective observation

TABLE 2. As in Table 1, but for wind at the CDA buoy given by MM5.

Class of wind direction θ_{REL} (°)		Class of wind velocity W (m s^{-1})					
		0–4	4–8	8–12	12–16	16–20	Percent
0.0–22.5	dw	7	2	0	0	0	*2.4*
22.5–67.5	dcw	24	10	5	2	0	*11.1*
67.5–112.5	cw	60	142	48	4	0	*68.5*
112.5–157.5	ucw	37	22	0	0	0	*15.9*
157.5–180.0	uw	8	0	0	0	0	*2.2*
	Percent	*36.7*	*47.4*	*14.3*	*1.6*	*0.0*	

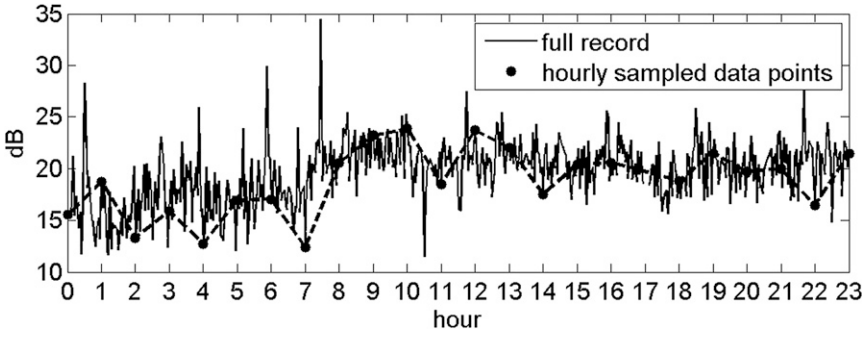

FIG. 7. An example of continuous recording of Z during 24 h and data points sampled for the present analysis.

domain. Figure 9 shows the evolution of this ratio over the time period under consideration. It can be seen that the values of C_Z and C_{VEL} remain close to each other and vary accordingly. Since the respective valid coverage have been determined with independent methods and since the variables themselves have been computed independently in the radar signal processing chain, this shows that the valid VEL and Z variables over the sea surface are closely related. They turn out to be simultaneously valid whenever Z is above the background noise level. Superimposed on the figure is the wind speed at the CDA buoy in open sea. Even though this measurement is relative to a single location in the radar coverage area, it can at least be considered as a qualitative parameter of the wind strength over that area. Time variations of the valid coverage for C_Z and C_{VEL} have a clear positive correlation with the wind speed.

4. Variation of radar parameters with wind and waves in the vicinity of the buoy

Radar parameters are compared to the wind and wave measurements at the location of the CDA buoy, which offers the most documented and reliable sea truth data. To reduce the noise level, the parameters have been averaged over 5 bins in range and 11 bins in azimuth, resulting in a surface area of $3.3 \times 3.4\,\mathrm{km}^2$. This area is close to the MM5 spatial resolution. As expected with the method used to estimate the radar parameters σ_Z, Z_{DR}, and VEL, the amount of valid measurements depends on the wind strength (Fig. 9). For example, 86% of measurements are valid for $W > 5\,\mathrm{m\,s^{-1}}$ and 64% for $W > 3\,\mathrm{m\,s^{-1}}$ (all winds: 50%). In the following a minimum wind velocity of $4\,\mathrm{m\,s^{-1}}$ has been retained.

a. Variations of radar cross section

The statistical distribution of σ_Z values has been derived for the different conditions of wind velocity W and relative wind direction θ_{REL} (Fig. 10a). The mean and standard deviations of σ_Z (dB) were computed for each class of $W - \theta_{\mathrm{REL}}$, with 2, 22, 173, 132, and 8 available samples for the dw, dcw, cw, ucw, and uw direction sectors, respectively. The results clearly show an increase of σ_Z with wind speed at a given θ_{REL}, typically of 15 dB from 5 to $14\,\mathrm{m\,s^{-1}}$ (cw), and an increase at given W as the wind direction evolves from down- to upwind, typically 8 dB from dcw to uw for $W = 8\,\mathrm{m\,s^{-1}}$. The variations of σ_Z with wind speed and direction do

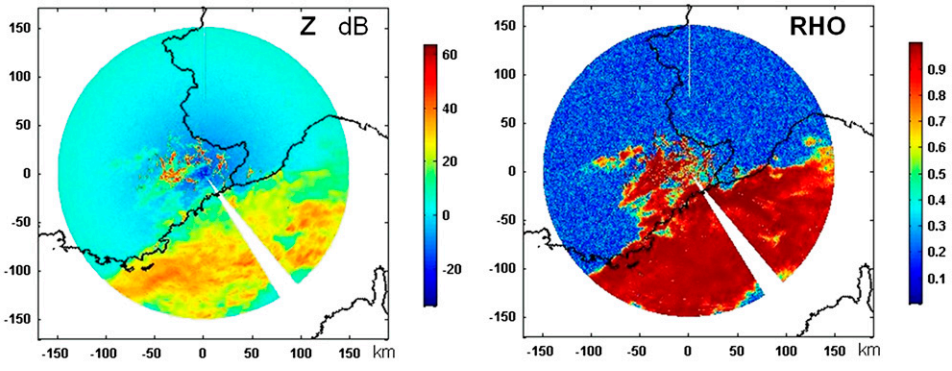

FIG. 8. Images of Z and RHO showing rain over the sea.

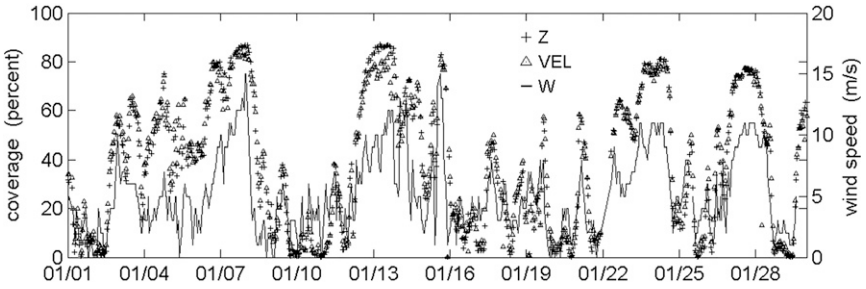

FIG. 9. Spatial coverage of Z (triangles), VEL (crosses), and wind speed at the CDA buoy.

not seem significantly different between wind sea-dominated (73% of σ_Z data for $W > 4\,\mathrm{m\,s^{-1}}$) and swell-dominated sea-state conditions (not shown here). This suggests that the variations of σ_Z with the wind vector are essentially due to the sensitivity of radar return to short-scale waves of the sea surface, which are known to be driven by the wind. However, the large dispersion of the values of σ_Z does not allow for drawing a definitive conclusion.

An empirical model can be obtained by a least squares fitting of the σ_Z data writing as

$$[\tilde{\sigma}_Z] = \sum_{i=0}^{2} (a_i \cos(\theta_{\mathrm{REL}}) + b_i)[W]^i, \qquad (9)$$

where [.] denotes the operator $10\log_{10}$ and θ_{REL} is in degrees, with the following coefficients: a0 = −9.27, b0 = −101.9; a1 = 1.00, b1 = 9.90; a2 = $-4.64\ 10^{-2}$, b2 = −0.36 for $4.5 < W < 17.7\,\mathrm{m\,s^{-1}}$; $6° < \theta_{\mathrm{REL}} < 176°$. The mean difference (MD), the root-mean-square difference (RMSD), and the correlation coefficient (CORR) between the modeled and measured σ_Z values are given in Table 3. The results are shown in Fig. 10b together with the predictions of the GIT sea clutter model in HH polarization (Horst et al. 1978; see the appendix). Note that, as there are very few σ_Z data at the CDA buoy for dw cases, the downwind curve obtained by Eq. (9) is an extrapolation of real data. We also report experimental values in X band and HH polarization by Nathanson (1991) and Hwang et al. (2008b). The grazing angles are 1° and 1.4°, respectively, which is close to our actual θ_g value. The Nathanson data are provided with respect to significant wave height. The outer limits of this range were converted to a range of equivalent Pierson–Moskowitz wind speeds and W was taken as the mean value. Note that the Nathanson data are omnidirectional. The Hwang et al. data were fitted by a linear polynomial regression. They correspond to the upwind direction. Our results are in qualitative good agreement with the GIT and Nathanson results. However, they overestimate the data given by Hwang et al. by about 10 dB. We also found good consistency in our results with recent measurements in X band and at near-grazing incidence angles by Plant et al. (2010) (not shown).

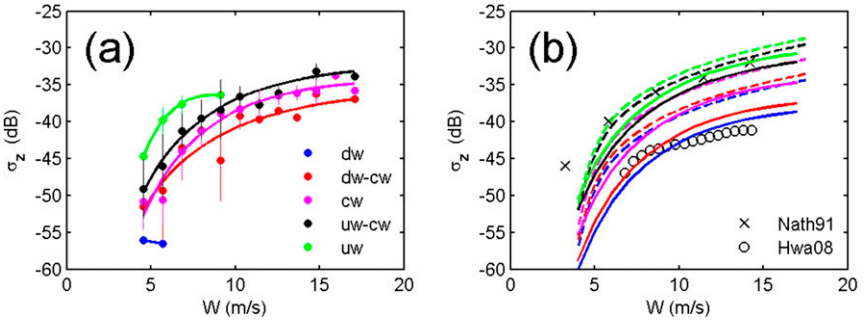

FIG. 10. Variation of σ_Z with wind speed for different classes of θ_{REL} (see Table 1). (a) Experimental data. Heavy dots refer to the mean values of σ_Z within given direction sectors, and vertical segments are delimited by mean value plus/minus standard deviation. The absence of a vertical segment indicates that only one measurement is available. Solid lines show the regression polynomials. (b) Empirical model (solid lines), GIT sea clutter model [dashed lines, same color conventions as in (a)], and measurements by Nathanson (1991) (crosses) and Hwang et al. (2008b) (circles).

TABLE 3. MD, RMSD, and CORR between modeled and measured σ_Z values regardless of the wind direction. Wind data are in situ measurements at the CDA buoy or estimates of MM5 (italic).

	MD (dB)		RMSD (dB)		CORR	
Empirical model Eq. (9)	−0.05		3.1		0.84	
GIT	2.7	*−2.7*	4.2	*5.6*	0.83	*0.45*
Modified GIT	0.3	*−5.7*	3.2	*7.6*	0.83	*0.41*

Variations of σ_Z with wind direction are monotonous from dw to uw direction. This behavior contrasts with that in VV, which is well known for presenting maxima of NRCS under uw and dw conditions, at least at moderate incidence angles (e.g., Stoffelen and Anderson 1997). Using X-band data at a low grazing angle, Guerraou et al. (2016) also observed a quasi-sinusoidal angular distribution in VV, whereas in HH the distribution shifts from two local maxima in uw and dw directions to a unique maximum in the uw direction as the grazing angle is decreased from 45° to 16°. Neglecting the cross-polarization contributions in Eq. (6) enables estimating the NRCS at VV polarization, σ_Z^{VV}, from Z_{DR} and σ_Z data (Fig. 11). Term σ_Z^{VV} is minimum in a broad sector from uw–cw to dw–cw, indicating a poor sensitivity to wind direction within this sector, and is maximum in the uw sector. It is not maximum in dw as expected, though it may be hazardous to draw any conclusion given the low number (two) of measurements within this sector.

The quantitative comparison of σ_Z with GIT simulations exhibits an overall (regardless of wind direction) overestimation of σ_Z by GIT (Table 3). A closer investigation shows that the MD varies from −0.6 to 7 dB depending on the wind direction sector. A better agreement with the GIT can be obtained using a modified directional term A_u [Eq. (A5)]:

$$A'_u = A_u \exp(-1.4 + 0.47\varphi). \tag{10}$$

The resulting GIT curves (not shown) are similar to Fig. 10b, except that the MDs between the model and experimental values are now smaller than 1.3 dB in absolute value.

The poorer agreement that is found between the modeled and measured σ_Z when MM5 wind estimates are used instead of the true wind vector reflects the differences in wind velocity outlined in section 2c. In particular, the MD values are consistent with an overall underestimation of σ_Z by the GIT model that is due to the underestimation of wind velocity by the MM5.

The fair agreement of the σ_Z–W variations with other data, including the GIT model results, reinforces the idea that σ_Z is a good estimation of the NRCS at HH polarization and grazing incidence.

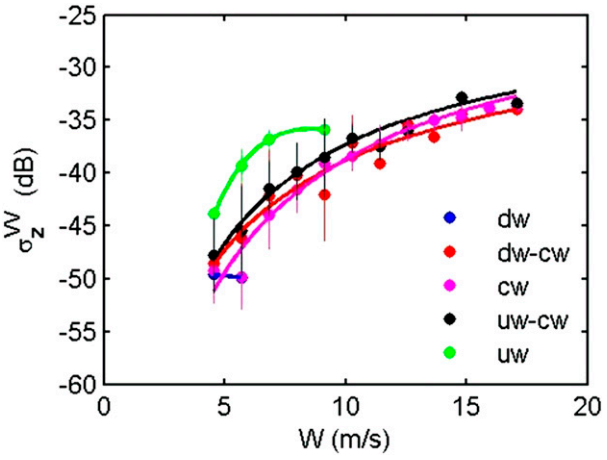

FIG. 11. As in Fig. 10a, but for VV polarization. Term σ_Z^{VV} is deduced from Z_{DR} and σ_Z according to Eq. (6).

b. Variations of the polarization ratio

The polarization ratio Z_{DR} (Fig. 12a) shows a weak dependency with respect to wind speed. It seems to undergo a small nonlinear variation in direction from the dw to the cw sector. Indeed, the mean Z_{DR} varies from −4.4 dB (sectors dw–dcw, 24 data points) to −2 dB (ucw–uw, 140 points) passing by −1.9 dB (cw, 173 points). Figure 12b compares the fourth degree polynomial regression of the data [applied to the Z_{DR} (dB) as for σ_Z] to Nathanson (1991) and Hwang et al. (2008b) measurements and to the GIT model prediction. A good general agreement is observed among these different data. In particular, as in several field measurements (e.g., Lee et al. 1995 in X band; Forget et al. 2006 in L band), the polarization ratio at near grazing is much higher than expected with the first-order scattering theory (Valenzuela 1978).

c. Variations of mean Doppler velocity

The variations of VEL with wind speed W are given in Fig. 13. The so-called Bragg velocities $\pm v_B$ (i.e., the phase velocities of the resonant short waves responsible for the backscatter) are also shown. We recall that v_B is given by

$$v_B = \sqrt{\frac{g}{k_B} + \frac{T_w}{\rho_w} k_B^3}, \tag{11}$$

where $k_B = 2k_i \cos\theta_g$; k_i is the radar wavenumber; and T_w and ρ_w are the seawater surface tension and density, respectively. At near-grazing angles one has $v_B \approx 0.23\ \mathrm{m\,s^{-1}}$. Figure 13a unveils a clear sensitivity of VEL to the wind direction and a slight variation with wind speed for a given wind sector. VEL is close

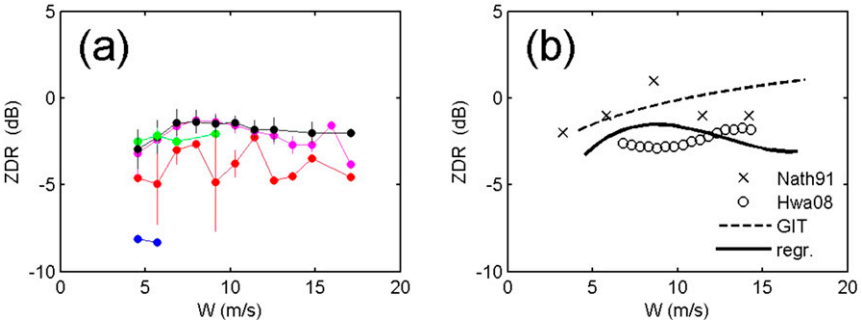

FIG. 12. Variation with wind speed of Z_{DR} for different classes of relative wind direction. (a) Experimental data. Symbols as in Fig. 10a. (b) Regression curve of experimental data (solid line), GIT sea clutter model (dashed line), and measurements by Nathanson (1991) (crosses) and Hwang et al. (2008b) (circles).

to $-v_B$ in dw–cw conditions ($-0.27\,\mathrm{m\,s^{-1}}$), slightly higher than $+v_B$ in cw conditions ($0.73\,\mathrm{m\,s^{-1}}$) and becomes significantly larger than v_B when the wind turns to upwind. This observation is consistent with the phenomenon of ''fast scatterers,'' which has been often pointed out at HH polarization and near-grazing incidence (see section 1). Even though there are only few data in the downwind sector, a tendency for asymmetry in VEL variations on both sides of the cw direction can be noticed. Furthermore, no visible influence of sea-state condition (swell or wind-wave dominated) can be inferred from the data. The data compare well with Hwang et al. (2008b) and Pidgeon (1968) (not shown here) obtained at near-grazing angle in C band. Recall that the dependency of VEL on the viewing angle of the radar relative to wind and waves was first observed by Pidgeon (1968).

The VEL parameter can be fitted to a linear function of W for each wind sector (as was done for σ_Z) with an RMSD value of $0.28\,\mathrm{m\,s^{-1}}$ regardless of the wind direction. However, a better representation is obtained using a linear dependence on the radial component of the wind speed rather than W (Fig. 13b):

$$\mathrm{VEL} = 0.62 + 0.19 W_r, \tag{12}$$

with an RMSD of $0.25\,\mathrm{m\,s^{-1}}$. The range of variation of W and θ_{REL} is the same as for Eq. (9). Here W_r is the component of the wind vector along the radar line of sight with the same sign convention as VEL; that is, W_r is positive whenever the wind component is orientated toward the radar. This result recalls the HF radar probing technique that measures the radial components of the surface current field (e.g., Barrick et al. 1977). It provides a new perspective on the use of two microwave radars to map the wind field in a manner similar to what is done with HF radars to map surface currents. Note that Eq. (12) was obtained for wind velocities greater than $4\,\mathrm{m\,s^{-1}}$. The offset of 0.62 in Eq. (12), which is 2 times larger than v_B, reflects the aforementioned upwind–downwind asymmetry. In upwind conditions ($W_r = W$), Eq. (12) can

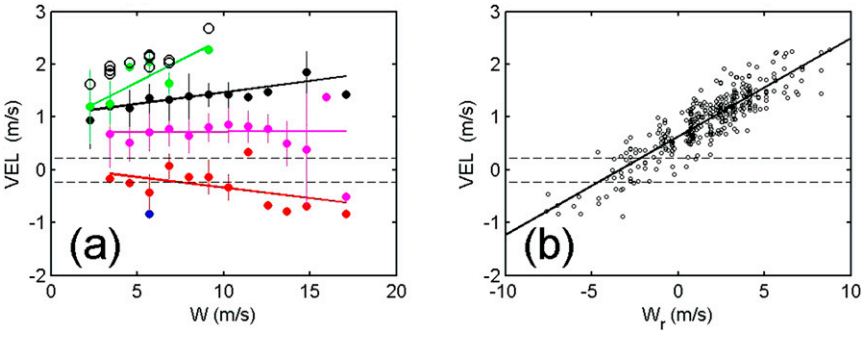

FIG. 13. Variation of VEL with wind speed. (a) Variations for different classes of relative wind direction. Solid lines denote linear regression. Bragg velocities are drawn as horizontal dashed lines. Other symbols as in Fig. 10a. The open circles reproduce measurements of Hwang et al. (2008b). (b) Variation with the radial wind velocity component. The solid line is the linear regression line.

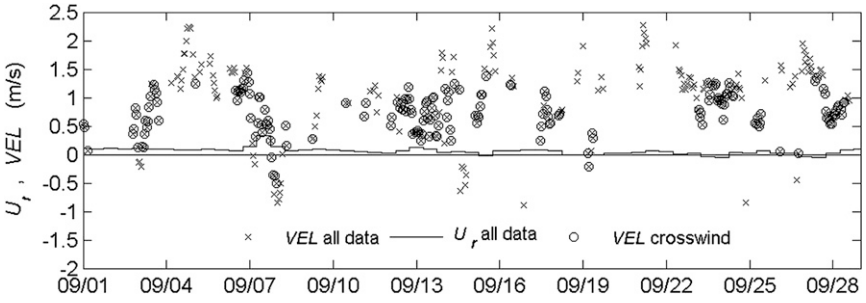

FIG. 14. Comparison of hourly sampled VEL measurements and radial surface current component U_r (12-h averaging). Crosswind cases are highlighted with circles.

be compared to the empirical relationship proposed by Hwang et al. (2008a):

$$c_s = 1.8p^{0.16}, \quad p = \frac{W^2}{gH_s}, \tag{13}$$

where c_s corresponds to the VEL parameter in breaking conditions. Equation (13) was obtained for $4 < p < 12$. We found a single value of p falling in this range ($p = 12$) giving VEL = 2.2 m s^{-1}, which is close to the model prediction (2.7 m s^{-1}). In the other cases ($1.7 < p < 3.3$), the VEL values are also in good agreement with the model (relative difference smaller than 33%), which suggests the validity of Eq. (12) in the range $1.7 < p < 12$. We think that the discrepancy between the VEL and c_s values is related to the restriction of Eq. (13) to breaking wave conditions.

An important issue is the possible influence of surface currents on the relationship between VEL and W_r. Figure 14 compares VEL and the radial component of the surface currents, U_r, computed by the circulation model and emphasizes the crosswind cases. VEL is in general significantly larger than U_r (with a mean absolute difference of 0.94 m s^{-1}) even in cw conditions. For this latter case, it was noticed that VEL shows on average a slight deviation from v_B (0.5 m s^{-1}). According to the first-order scattering theory used for HF radars (Barrick et al. 1977), this deviation should be equal to U_r if it were due to surface currents. Yet, the actual values of U_r are smaller (0.09 m s^{-1} on average). This suggests that in the present experiment, the contribution of surface currents to VEL is weak and that the relationship Eq. (12) is acceptable. It can be also considered that the wind-induced (Ekman) current component is directly related to W_r and therefore that the VEL–W_r relationship already contains this wind–current dependence. In other oceanographic conditions—for example, in coastal zones with strong tidal currents—surface currents are likely to be taken into account.

d. Wind inversion

The empirical models Eqs. (9) and (12) are used jointly for the retrieval of wind velocity and relative direction. The inverted values $W^{(\mathrm{inv})}$ and $\theta_{\mathrm{REL}}^{(\mathrm{inv})}$ have been compared to the field measurements W and θ_{REL}, respectively, in Fig. 15. Term W_{inv} is generally larger than 4 m s^{-1} (minimum value of 3.6 m s^{-1}), which reflects the fact that radar parameters are not valid at low winds. Only 49% of the valid values of σ_Z and VEL could be inverted. However, despite the shortcomings of the inversion, which are mainly due to the statistical variability of the radar measurements, the retrieved wind captures well the temporal variations of the actual wind (not shown). The mean difference between the inverted and measured wind speed (relative direction) is 0.4 m s^{-1} (−1°) with an RMSD error of 1.7 m s^{-1} (16°).

A theoretical study has been performed to estimate the error on inverted wind parameters that can be ascribed to the nonlinearity of the system of Eqs. (9) and (12), given the statistical variability of σ_Z and VEL. For this, we simulate independent realizations of random variables X_1 and X_2, representing the radar parameters σ_Z and VEL, respectively, with uniform distribution. The mean M_i and standard deviation S_i were calculated from radar measurements within classes of W–θ_{REL} as in sections 4a and 4b, centered on W^c–θ_{REL}^c with widths of 3 m s^{-1} and 45°, respectively. A minimum of 20 measurements per class was sought to ensure accurate estimates of M_i and S_i. This condition was satisfied for cw and ucw wind direction sectors, with W ranging from 3 to 15 m s^{-1}. The inversion of Eqs. (9) and (12) based on the average values M_i yields to an estimation of the wind parameters in good agreement with the actual W^c and θ_{REL}^c values, with differences of 3.6% and 5.7%, respectively. To check the variability of the inversion procedure, we used 225 realizations of (X_1, X_2) within each class to evaluate the statistics of the wind parameters W and θ_{REL}. We found an average bias of 0.4 m s^{-1} and −4° for wind speed and direction, respectively, with respect to the

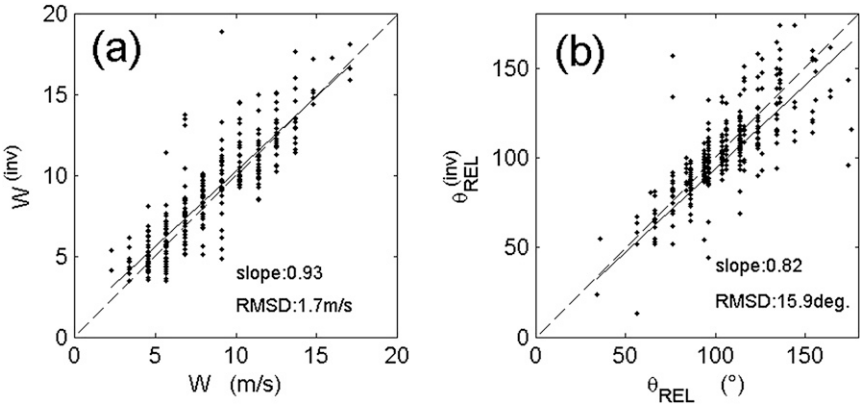

FIG. 15. Inversion of (a) wind speed and (b) relative direction at the CDA buoy from empirical models Eqs. (9) and (12), respectively. The regression and identity lines are shown in solid and dashed lines, respectively.

actual values of W^c and θ^c_{REL}, with corresponding standard deviations of 1.9 m s^{-1} and 16°. These values are found very close to the values obtained from the times series analysis given above. We conclude that the observed statistical variability of σ_Z and VEL measurements does not significantly deteriorate the quality of the inversion.

The satisfactory performance of the wind inversion at the CDA buoy was to be expected, since the models have been established using radar and wind measurement at this location. The RMSD values are reasonably low given the selected dataset, which is noisy at the chosen sampling rate of 1 h (see section 3; Fig. 7). The good agreement found between inverted wind parameters from radar parameters averaged within wind classes suggests that the use of the complete data at a nominal sampling of 170 s would enable diminishing the noise by appropriate preprocessing (e.g., smoothing, filtering). This is left for future work.

5. Spatial properties of NRCS and VEL

a. NRCS

The examination of NRCS maps reveals in most cases (see Fig. 4e) a systematic decrease of the signal at large distances and a systematic variation in gain with azimuth ϕ (referred to as the west–east axis). This is confirmed in Fig. 16a, which depicts the variations of the NRCS with ϕ of σ_Z, after averaging over 10-km-wide range bins centered on nine increasing distances. We have investigated in more detail the variations that are not due to wind or sea state. To this aim, we have assumed that the sensitivity of the NRCS to the wind vector is spatially homogeneous and is described by the GIT model. The use of the latter is justified by its good performance obtained at the CDA buoy. The geophysical contribution of wind to σ_Z was removed using wind velocities and directions taken from MM5 results, the only available data that can describe the spatial variability of the wind field. Cases of low-wind (<4 m s^{-1}) velocity were discarded in the analysis. The result of this wind filtering procedure was quantified by the so-called residual function $S(r, \phi) = \sigma_Z/\sigma^{(\mathrm{MM5})}_{\mathrm{GIT}}$, where $\sigma^{(\mathrm{MM5})}_{\mathrm{GIT}}$ is the NRCS value derived from the GIT model using MM5 wind prediction. The modified GIT model is considered [Eq. (10)].

Function S is shown in Fig. 16b with the same range averaging as in Fig. 16a. The general picture is an azimuthal variation of S that is nearly independent of range, from $r_1 = 70$ km to $r_2 = 110$ km. Variations in range are observed at other distances (dashed–dotted and dotted lines in the figure) and at extreme azimuths ($\phi > \phi_1 = -108°$ and $\phi < \phi_2 = -35°$). The values of r_1, r_2, ϕ_1, and ϕ_2 were determined from the spreading of the probability distribution function (PDF) of S computed over all ranges for each azimuth. The obtained values bound the domain for which the PDF is narrow enough to assume that variations of S with range are small. The mean residual function, $\langle S \rangle$, averaged over the interval (r_1, r_2) is shown in the same figure. A close examination of the topography along the azimuthal bearings allows one to interpret the large variations of S and $\langle S \rangle$ outside the interval (ϕ_1, ϕ_2) by shadowing effects. However, these effects do not explain the minima observed in the vicinity of particular azimuths, for example, at $\phi = -78°$ and $\phi = -89°$. There is an overall underestimation of the NRCS by the GIT model, equal to 4.7 dB at the CDA buoy, that can be explained by the underestimation of the wind speed by MM5 (Fig. 6). Indeed, using Eq. (8), the underestimation of NRCS is considerably reduced, by 5.7 dB, at the CDA buoy.

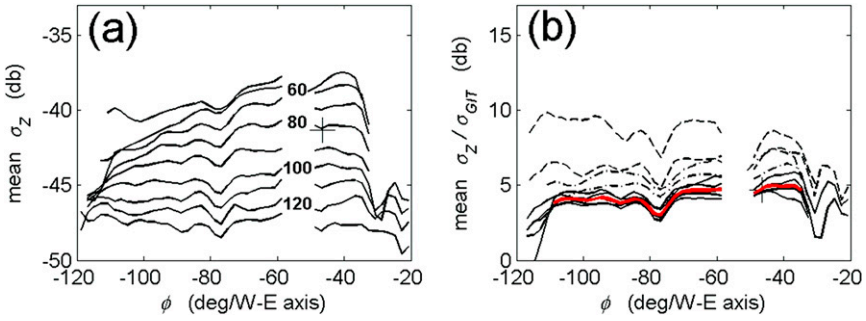

FIG. 16. (a) Variation with distance r and azimuth ϕ of the mean NRCS. For a given ϕ the average is performed over consecutive 10-km-wide range intervals from 50 to 130 km. The crosses indicate the σ_Z values at the CDA buoy location (at a distance of 79 km from the radar). (b) Variation of the mean residual function S for the same consecutive intervals as in (a). Dashed–dotted lines correspond to $r < 70$ km and dashed line corresponds to $r > 110$ km. The curve in red is the mean of S for $70 < r < 110$ km and $-108° < \phi < -35°$. The value at the buoy is marked by a cross.

The mean residual function $\langle S \rangle$ will be applied to NRCS measurements for inversion purposes.

b. VEL

This parameter has been submitted to a similar analysis to study the spatial variability of VEL and the residual V defined as the difference between VEL and $\text{VEL}_{\text{mod}}^{(\text{MM5})}$ given by Eq. (12), where the radial component of the wind along the radar bearing is estimated from MM5 wind simulations. The variations with ϕ of range-averaged VEL for increasing distances are shown in Fig. 17. Contrary to the NRCS, these variations generally show a small dependency on distance except, as for the NRCS, within some regions, especially at extreme azimuths. We will restrict the analysis to the interval ϕ_1–ϕ_2 defined in section 4b. The observed trends in azimuthal variations are similar to the mean curve, $\langle \text{VEL} \rangle$, obtained by range averaging (red solid line). The mean residual $\langle V \rangle$, drawn in the red dashed line, is very low and is slightly flatter than $\langle \text{VEL} \rangle$. However, $\langle V \rangle$ shows a similar azimuthal variation that can be attributed to the moderate performance of the MM5 meteorological model.

However, despite the lack of precision of MM5 data, we can refer to these data to illustrate one of the main results of the present study; that is, radar VEL measurements are linearly related through Eq. (12) to the radial component of the surface wind W_r. Figure 18 illustrates the remarkable similarity between concurrent maps of model-derived radial wind speed $W_r^{(\text{MM5})}$ and radar-derived radial wind speed $W_r^{(\text{VEL})}$ for west (Figs. 18a,b, respectively) and east–northeast (Figs. 18c,d) wind regimes. Term $W_r^{(\text{VEL})}$ was obtained from radar measurements of VEL projected onto the model grid by interpolation. The correlation coefficients are 0.95 and 0.91, respectively, and the slopes (SL) of the linear regression are 1.16 and 1.98 for $W_r^{(\text{MM5})}$ and $W_r^{(\text{VEL})}$, respectively. Since the wind velocity is quite homogeneous in the area under study (standard deviation of about 1 m s^{-1}), the high values of CORR suggest: first, that the spatial distribution of $W_r^{(\text{VEL})}$ reflects that of $\theta_{\text{REL}}^{(\text{MM5})}$; and, second, that $\theta_{\text{REL}}^{(\text{MM5})}$ is a good estimate for θ_{REL}. There are some cases of homogeneous wind velocity for which $W_r^{(\text{VEL})}$ and $W_r^{(\text{MM5})}$ distributions are different, with strong evidence that $W_r^{(\text{VEL})}$ reflects the true wind direction. An example is depicted in Fig. 19b, where the $W_r^{(\text{VEL})}$ distribution is consistent with a wind blowing from the west rather than from the northwest as predicted by MM5 (Fig. 19a). The wind direction from the west was indeed recorded by the meteorological stations IL and FR indicated in Fig. 19a (see also Fig. 2).

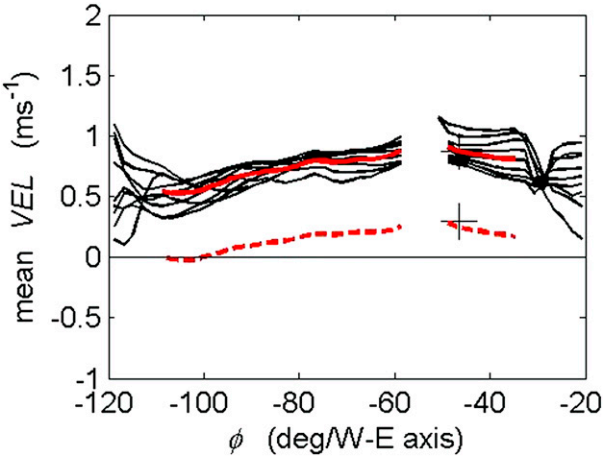

FIG. 17. Variation of the mean Doppler velocity with distance and azimuth. The averaging procedure is as in Fig. 16. Solid red line is the average of these variations in the interval of azimuth $-108° < \phi < -35°$. Dashed red line is the average of the residual $\langle V \rangle$ between the measured and modeled VEL. Crosses indicate the values at the CDA buoy location.

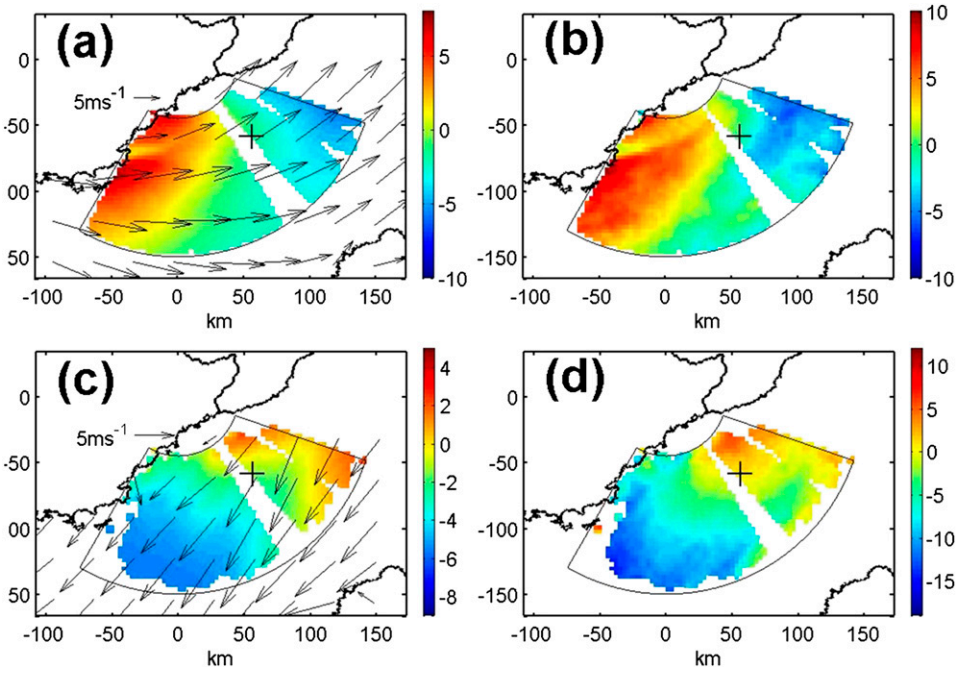

FIG. 18. Concurrent maps of radial wind from (a),(c) MM5 and (b),(d) the radar measurements of VEL using Eq. (12) at two dates with different wind regimes: (a),(b) 7 and (c),(d) 9 Sep. Model wind vectors sampled every 10 nods are drawn in (a),(c). The crosses indicate the location of the CDA buoy.

Note that for this particular day, the wind directions at the CDA buoy and from MM5 agree within 20°.

A linear regression analysis was performed between $W_r^{(\mathrm{MM5})}$ and $W_r^{(\mathrm{VEL})}$ for the whole dataset with the constraint that wind velocity as given by MM5 is larger than $4\,\mathrm{m\,s^{-1}}$ (Table 4). Given the uncertainties of MM5 wind estimates, CORR and SL values support our model of VEL. The results of the comparison between $\theta_{\mathrm{REL}}^{(\mathrm{MM5})}$ and $W_r^{(\mathrm{VEL})}$ on the one hand, and $W^{(\mathrm{MM5})}$ and $W_r^{(\mathrm{VEL})}$ on the other hand, show that the relatively high correlation obtained between $W_r^{(\mathrm{MM5})}$ and $W_r^{(\mathrm{VEL})}$ is mainly due to the high correlation between $\theta_{\mathrm{REL}}^{(\mathrm{MM5})}$ and $W_r^{(\mathrm{VEL})}$, whereas the sensitivity of $W_r^{(\mathrm{VEL})}$ to variations of the sole wind velocity is hardly detectable.

c. *Wind field inversion*

The principle of the derivation of wind parameters from radar measurements is the same as in section 3d [use of the empirical models Eqs. (9) and (12)], except that one should filter out from the radar signal the spatial variations that are not related to wind. We found in section 4a that this correction is important for σ_Z. The inversion procedure holds over a domain defined by ranges r_1–r_2 and azimuths ϕ_1–ϕ_2 and consists of two steps. First, a correction is applied to σ_Z:

$$\sigma'_Z = \sigma_Z - \langle S\rangle + \langle S\rangle_{\mathrm{CDA}}, \tag{14}$$

where $\langle S\rangle_{\mathrm{CDA}}$ is the value of the residual function $\langle S\rangle$ at the CDA buoy. Equation (14) implies that σ'_Z and σ_Z coincide at the CDA buoy. The inverted wind speed $W^{(\mathrm{inv})}$ and $\theta_{\mathrm{REL}}^{(\mathrm{inv})}$ are then obtained by solving

$$[\sigma'_Z] - \sum_{i=0}^{2}\left[a_i\frac{W_r}{W^{(\mathrm{inv})}} + b_i\right][W^{(\mathrm{inv})}]^i = 0 \tag{15}$$

with $W_r = (\mathrm{VEL} - 0.62)/0.19$ and

$$\theta_{\mathrm{REL}}^{(\mathrm{inv})} = \cos^{-1}(W_r/W^{(\mathrm{inv})}). \tag{16}$$

When applied to radar measurements at the CDA buoy, this procedure gives identical results to those presented in section 3d. Because of the noise of radar data, the use of Eqs. (15) and (16) produce imaginary solutions in 32% of cases on average. For the valid cases, the inverted wind parameters are compared with the MM5 predictions in Fig. 20. The mean values of $W^{(\mathrm{inv})}$ and $\theta_{\mathrm{REL}}^{(\mathrm{inv})}$ over the inversion domain (Figs. 20a,b) exhibit the same temporal variations as the corresponding MM5 parameters. Inverted wind speeds are often larger than MM5 estimates, for example, 6–8, 22–24, and 27–28 September. We put this on the account of the poor performance of MM5 to reproduce accurate wind speed estimates, as already mentioned, rather than the inversion procedure itself. To support this assumption, note that whenever the wind speed is overestimated with respect to MM5,

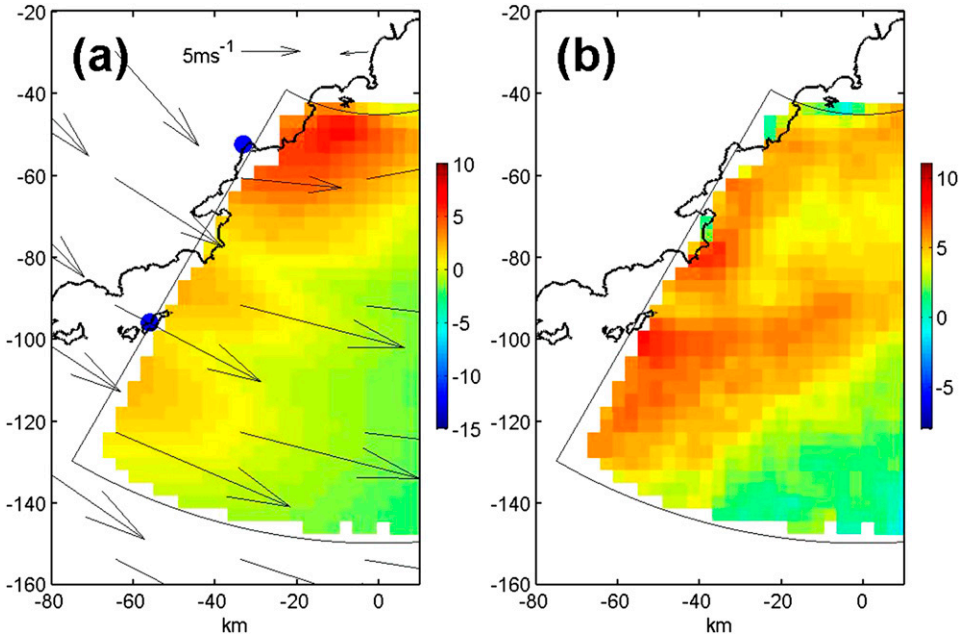

FIG. 19. As in Fig. 18, but for 13 Sep with a focus on the western part of the observation domain. Meteorological stations are marked in blue (see Fig. 2).

$W^{(\mathrm{inv})}$ is close to wind speed measurements at the CDA buoy, which is in the central part of the domain. The overall comparison between $W^{(\mathrm{inv})}$ and $W^{(\mathrm{MM5})}$ is shown in Figs. 20c,d. The density shown with contour lines in Figs. 20c,d is defined as the percentage of samples of wind speed (direction) counted in small grid squares, $1 \times 1\,\mathrm{m\,s^{-1}}$ (5° × 5°) referred to as the number maximum equal to 93 923. A minimum density of 0.2% is considered in such a way that the data of higher density represent more than 70% of the total number. The picture for wind speed is the same as before, that is, $W^{(\mathrm{inv})}$ values overestimate $W^{(\mathrm{MM5})}$. Relative wind directions agree well with each other.

6. Conclusions

We have investigated the signature of the sea surface from the images collected by an X-band conventional weather radar and its potential application to marine remote sensing of the coastal zone. The reflectivity factor Z provided by the meteorological software was converted into a sea normalized radar cross section σ_Z according to the radar equation; the differential reflectivity Z_{DR} was identified to the polarization ratio and the mean radial velocity VEL to the mean Doppler velocity induced by the sea scatterers. The copolarized correlation coefficient RHO was used to filter out rain. The radar data used in this study suffer from the statistical variability due to the chosen hourly sampling rate. The use of the full dataset (24 mappings per hour), which is left for future work, should considerably reduce this variability.

The analysis of σ_Z in the vicinity of a buoy providing surface wind and wave measurements has shown clear variations of σ_Z with respect to wind speed and relative wind direction, which are consistent with the GIT model at near-grazing angle and measurements found in the literature. The agreement of σ_Z with the GIT model is even better if the directional term of this model is slightly modified. An alternative empirical model of σ_Z, more accurate than the modified GIT, has been developed. VEL measurements at the same location compare well with measurements made elsewhere and show that, as already reported in the literature, the Doppler shift in HH at near-grazing incidence can be much larger than the Doppler shift expected from the resonant Bragg waves. One of the main results of this study is the linear relationship between VEL and the radial component of the wind speed, for moderate to strong wind speeds, suggesting that a coherent weather radar can allow for the mapping of the surface wind over the sea at high spatial and temporal resolutions at a basin

TABLE 4. Mean CORR and SL of the linear regression between the radar-derived radial wind component $W_r^{(\mathrm{VEL})}$ and parameters derived by MM5. Standard deviations are given in italic. SL value is not useful for $\theta_{\mathrm{REL}}^{(\mathrm{MM5})}$ and $W^{(\mathrm{MM5})}$.

	CORR	SL
$W_r^{(\mathrm{MM5})}$	0.69 *0.27*	0.39 *0.19*
$\theta_{\mathrm{REL}}^{(\mathrm{MM5})}$	0.65 *0.26*	—
$W^{(\mathrm{MM5})}$	−0.09 *0.42*	—

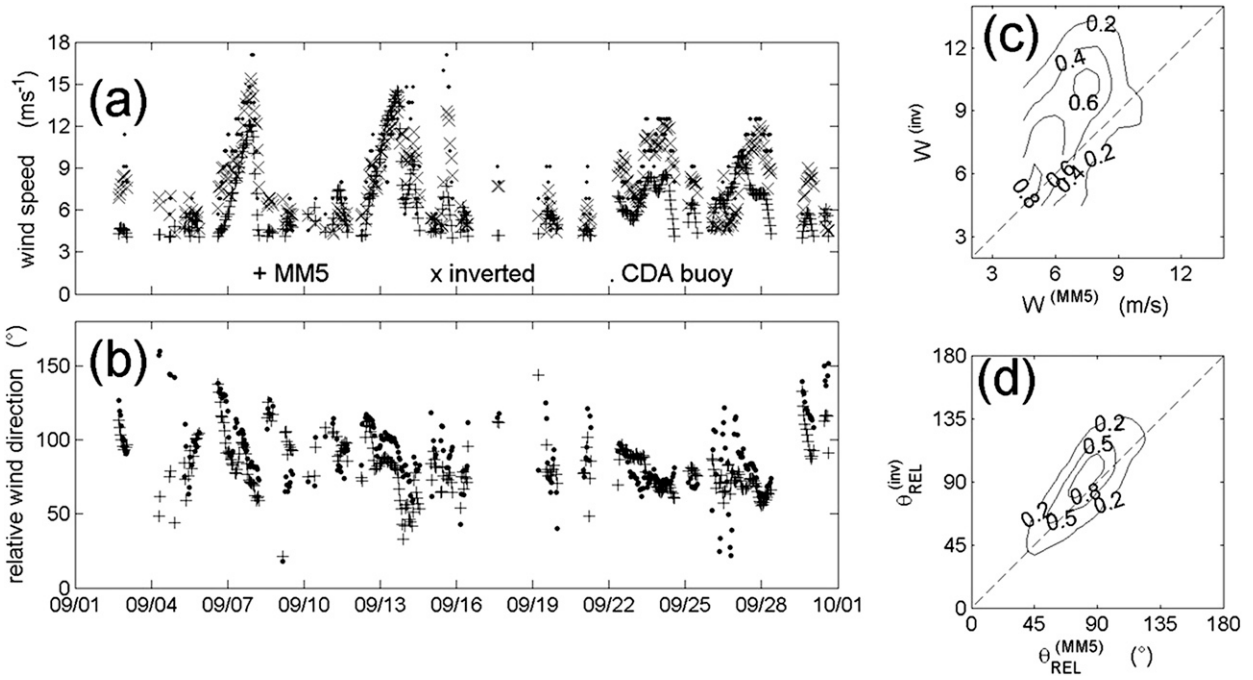

FIG. 20. Comparison between (a),(c) MM5-derived and inverted wind velocity and (b),(d) relative direction. (a),(b) Averages over the radar coverage; (c),(d) density contours. Regression (solid) and identity (dashed) lines are shown together with correlation parameters.

scale. This performance is similar, in terms of resolution and range, to the mapping of radial surface current by HF radars. Therefore, two distant weather radars installed near the shore potentially allow the monitoring of the wind vector field. The influence of surface currents has been investigated for VEL data in the vicinity of the buoy. It is negligible in the present experiment but could be significant in other places where currents are stronger and should be taken into account, for example, using the data of an operational circulation model.

The analysis of radar measurements has been extended to the entire coastal zone using the wind estimates of a high-resolution meteorological model (MM5). Results similar to those obtained for σ_Z and VEL near the meteorogical buoy have been obtained with significantly lower accuracy, particularly due to the moderate performance of MM5. Another reason for this deterioration of performance comes from processes related to, for example, topography and propagation at long range, which are not dependent on the wind field and which impact the spatial distribution of σ_Z and, to a lesser extent, VEL. For σ_Z we could define a limited zone in range and azimuth within which it was possible to calculate a mean variation with azimuth (called mean residual function), independent of range. The influence of the topography on this function was identified. The maps of radial wind derived from VEL data are generally close to MM5 predictions and, in some cases, better resolved and more accurate. However, because of the performance of MM5, the sensitivity of the derived radial wind speeds to sole wind velocity was difficult to detect.

Since the NRCS of the sea surface is sensitive to both wind direction and intensity, while VEL is related to the radial surface wind component, it is in principle possible to invert the wind vector from radar measurements. Wind inversion, which not surprisingly gives good results at the buoy position, has been extended to the entire radar coverage using the empirical relationships $\sigma_Z(W, \theta_{\mathrm{REL}})$ and $\mathrm{VEL}(W_r)$ after correction of σ_Z values by the mean residual function. Given the limits of accuracy of MM5 and the level of noise of radar data, the results are encouraging.

These preliminary results pave the way for the concept of weather radar for ocean remote sensing. In the first step, the parameter VEL, which contains the information about the radial wind, is sufficient to map the radial wind (and possibly also the wind vector using two distant radars). However, to establish the universality of the relationship $\mathrm{VEL}(W_r)$ [Eq. (12)], which was obtained empirically at a given radar bin, would require a specific and detailed study, including theoretical developments and experimental assessment. The second step is the simultaneous use of parameters σ_Z and VEL, which allow mapping of the wind vector field. In this case, the relationship $\sigma_Z(W, \theta_{\mathrm{REL}})$ [Eq. (9)] should be studied as well, but we

have shown that a classical model such as GIT provides a suitable first-guess relationship.

The main issue with the parameter σ_Z is its sensitivity to instrumental artifacts and other effects not related to the wind. These artifacts either reduce the spatial domain of application of the inversion method or make calibration necessary. In the present study this spatial domain is limited to a maximum range of 110 km. Above this distance the signal decays more rapidly than predicted by the GIT model. This suggests that, because of unknown refraction effects, propagation at long range cannot be reproduced in a simple manner without ancillary information on, for example, air–sea temperature and water vapor. We think that this issue of calibration or correction of NRCS measurements necessitates specific studies. For example, for operational purposes, it would be interesting to dispose of data provided by a meteorological model allowing for estimation of a realistic refraction index over the working area. We did not exploit in this paper all the available parameters provided by the radar, especially the polarimetric parameter Z_{DR}. The improvement brought by this additional parameter should be investigated in further studies.

The data used in this study are available for verification purposes upon request from the corresponding author.

APPENDIX

GIT Model

The GIT model writes at HH polarization and for the actual radar wavelength (Horst et al. 1978 from Long 2001):

$$\sigma_{\mathrm{GIT}} = A_g A_i A_u A_w, \tag{A1}$$

$$A_g = 1.26 \times 10^{-7} \theta_g^{0.4}, \tag{A2}$$

$$A_i = \frac{m^4}{1+m^4} \quad m = 184.7 \theta_g h_{\mathrm{av}}, \tag{A3}$$

$$A_u = \exp\{-(0.68 - 1.9\theta_g)\cos\theta_{\mathrm{REL}}\}, \quad \text{and} \tag{A4}$$

$$A_w = \left(\frac{1.94W}{1+0.06W}\right)^{3.73}, \tag{A5}$$

where h_{av} is the average wave height ($=0.64\ H_s$). The product $A_g A_i$ simulates the overall variation of the NRCS with range or grazing angle, including multipath interference effects. Terms A_w and A_u express the dependency of the NRCS on wind speed and direction, respectively. For θ_g varying between 1.79° and 0.09° (r = 45.6 km and 150 km), A_u can be approximated by

$$A_u = \exp(-0.66\cos\theta_{\mathrm{REL}}) \tag{A6}$$

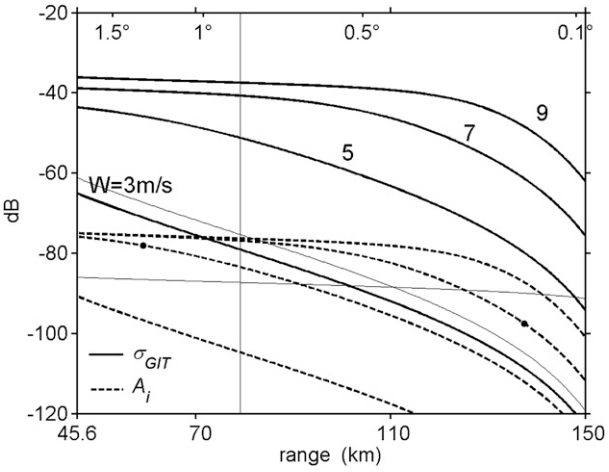

FIG. A1. Variation of σ_{GIT} with distance (heavy solid lines) and A_i (dashed lines) for various wind speeds and a cw direction. The horizontal axis is limited by the range of distances ($r_{\min}$, $r_{\max}$) considered in this study. The vertical line indicates the distance to the CDA buoy. Dots on the curves correspond to r_c. Variations in $\theta_g^{0.4}$ and $\theta_g^{4.4}$ are drawn with thin solid lines (with arbitrary amplitude).

with a relative uncertainty smaller than 4%. Taking θ_g between 1.03° and 0.44° (r varying between r_1 =70 km and r_2= 110 km; see section 4a), this value becomes 1%.

Let r_c be defined as

$$r_c = \pi \frac{hH_s}{\lambda} = 1.5110^3 H_s, \tag{A7}$$

where r_c is a typical ''critical'' distance of transition between a plateau region, where NRCS changes slowly with increases in r (decreases in θ_g), and the near-grazing incidence region, where NRCS decreases rapidly due to an interference effect between direct and reflected electromagnetic waves (Fig. A1). Term σ_{GIT} varies as $\theta_g^{0.4}$ in the plateau region and as $\theta_g^{4.4}$ at near grazing.

REFERENCES

Alves, H. G. M., M. L. Banner, and I. R. Young, 2003: Revisiting the Pierson–Moskowitz asymptotic limits for fully developed wind waves. *J. Phys. Oceanogr.*, **33**, 1301–1323, doi:10.1175/1520-0485(2003)033<1301:RTPALF>2.0.CO;2.

Barrick, D. E., M. W. Evans, and B. L. Weber, 1977: Ocean surface currents mapped by radar. *Science*, **198**, 138–144, doi:10.1126/science.198.4313.138.

Bringi, V. N., and V. Chandrasekar, 2001: *Polarimetric Doppler Weather Radar: Principles and Applications*. Cambridge University Press, 636 pp.

Dagestad, K.-F., and Coauthors, 2013: Wind retrieval from synthetic aperture radar—An overview. *Proceedings of SeaSAR 2012*, L. Ouwehand, Ed., European Space Agency Publ. SP-709, 22 pp.

Dankert, H., J. Horstmann, and W. Rosenthal, 2003: Ocean wind fields retrieved from radar-image sequences. *J. Geophys. Res.*, **108**, 3352, doi:10.1029/2003JC002056.

Doviak, R. J., and D. S. Zrnić, 1984: *Doppler Radar and Weather Observations*. Academic Press, Inc., 458 pp.

Forget, P., M. Saillard, and P. Broche, 2006: Observations of the sea surface by coherent L band radar at low grazing angles in a nearshore environment. *J. Geophys. Res.*, **111**, C09015, doi:10.1029/2005JC002900.

Gregers-Hansen, V., and R. Mital, 2012: An improved empirical model for radar sea clutter reflectivity. *IEEE Trans. Aerosp. Electron. Syst.*, **48**, 3512–3524, doi:10.1109/TAES.2012.6324732.

Guerraou, Z., S. Angelliaume, L. Rosenberg, and C.-A. Guérrin, 2016: Investigation of azimuthal variations from X-band medium grazing angle sea clutter. *IEEE Trans. Geosci. Remote Sens.*, in press.

Guihou, K., J. Marmain, Y. Ourmières, A. Molcard, B. Zakardjian, and P. Forget, 2013: A case study of the mesoscale dynamics in the North-Western Mediterranean Sea: A combined data–model approach. *Ocean Dyn.*, **63**, 793–808, doi:10.1007/s10236-013-0619-z.

Haack, T., C. Wang, S. Garrett, A. Glazer, J. Mailhot, and R. Marshall, 2010: Mesoscale modeling of boundary layer refractivity and atmospheric ducting. *J. Appl. Meteor. Climatol.*, **49**, 2437–2457, doi:10.1175/2010JAMC2415.1.

Horst, M. M., F. B. Dyer, and M. T. Tuley, 1978: Radar sea clutter model. *Proceedings of the International Conference on Antennas and Propagation: Part 2*. Institution of Electrical Engineers, 6–10.

Hwang, P. A., M. A. Sletten, and J. V. Toporkov, 2008a: Analysis of radar sea return for breaking wave investigation. *J. Geophys. Res.*, **113**, C02003, doi:10.1029/2007JC004319.

——, ——, and ——, 2008b: Breaking wave contribution to low grazing angle radar backscatter from the ocean surface. *J. Geophys. Res.*, **113**, C09017, doi:10.1029/2008JC004752.

Kalmykov, A. I., and V. V. Pustovoytenko, 1976: On polarization features of radio signals scattered from the sea surface at small grazing angles. *J. Geophys. Res.*, **81**, 1960–1964, doi:10.1029/JC081i012p01960.

Le Bouar, E., J. Testud, and T. D. Keenan, 2001: Validation of the rain profiling algorithm ''ZPHI'' from the C-band polarimetric weather radar in Darwin. *J. Atmos. Oceanic Technol.*, **18**, 1819–1837, doi:10.1175/1520-0426(2001)018<1819:VOTRPA>2.0.CO;2.

Lee, P. H. Y., and Coauthors, 1995: X band microwave backscattering from ocean waves. *J. Geophys. Res.*, **100**, 2591–2611, doi:10.1029/94JC02741.

Long, M. W., 2001: *Radar Reflectivity of Land and Sea*. 3rd ed. Artech House Radar Library, Artech House, 534 pp.

Madec, G., 2008: NEMO ocean engine. Version 3.2, IPSL Tech. Rep. 27, 211 pp.

Meischner, P., 2004: *Weather Radars*. Springer-Verlag, 337 pp.

Miret, D., G. Soriano, F. Nouguier, P. Forget, M. Saillard, and C.-A. Guérin, 2014: Sea surface microwave scattering at extreme grazing angle: Numerical investigation of the Doppler shift. *IEEE Trans. Geosci. Remote Sens.*, **52**, 7120–7129, doi:10.1109/TGRS.2014.2307893.

Mouche, A. A., F. Collard, B. Chapron, K.-F. Dagestad, G. Guitton, J. A. Johannessen, V. Kerbaol, and M. W. Hansen, 2012: On the use of Doppler shift for sea surface wind retrieval from SAR. *IEEE Geosci. Remote Sens.*, **50**, 2901–2909, doi:10.1109/TGRS.2011.2174998.

Nathanson, F. E., 1991: *Radar Design Principles: Signal Processing and the Environment*. 2nd ed. McGraw-Hill, Inc., 733 pp.

Nwogu, O. G., and D. R. Lyzenga, 2010: Surface-wavefield estimation from coherent marine radars. *IEEE Trans. Geosci. Remote Sens. Lett.*, **7**, 631–635, doi:10.1109/LGRS.2010.2043712.

Ourmières, Y., B. Zakardjian, K. Béranger, and C. Langlais, 2011: Assessment of a NEMO-based downscaling experiment for the North-Western Mediterranean region: Impacts on the Northern Current and comparison with ADCP data and altimetry products. *Ocean Modell.*, **39**, 386–404, doi:10.1016/j.ocemod.2011.06.002.

Pidgeon, V. W., 1968: Doppler dependence of radar sea return. *J. Geophys. Res.*, **73**, 1333–1341, doi:10.1029/JB073i004p01333.

Plant, W. J., W. C. Keller, K. Hayes, and G. Chatham, 2008: Measuring and modeling the NRCS of the sea for backscatter. *2008 IEEE International Geoscience and Remote Sensing Symposium: Proceedings*, Vol. 4, IEEE, IV-65–IV-68, doi:10.1109/IGARSS.2008.4779657.

——, ——, ——, and ——, 2010: Normalized radar cross section of the sea for backscatter: 1. Mean levels. *J. Geophys. Res.*, **115**, C09032, doi:10.1029/2009JC006078.

Rozenberg, A. D., D. C. Quigley, and W. K. Melville, 1996: Laboratory study of polarized microwave scattering by surface waves at grazing incidence: The influence of long waves. *IEEE Geosci. Remote Sens.*, **34**, 1331–1342, doi:10.1109/36.544557.

Scott, R. D., P. Krehbiel, and W. Rison, 2001: The use of simultaneous horizontal and vertical transmissions for dual-polarization radar meteorological observations. *J. Atmos. Oceanic Technol.*, **18**, 629–648, doi:10.1175/1520-0426(2001)018<0629:TUOSHA>2.0.CO;2.

Sirkova, I., 2011: Propagation factor and path loss simulation results for two rough surface reflection coefficients applied to the microwave ducting propagation over the sea. *Progr. Electromag. Res.*, **17M**, 151–166, doi:10.2528/PIERM11020602.

Skolnik, M., 1980: *Introduction to Radar Systems*. McGraw-Hill, Inc., 580 pp.

Stoffelen, A., and D. Anderson, 1997: Scatterometer data interpretation: Measurement space and inversion. *J. Atmos. Oceanic Technol.*, **14**, 1298–1313, doi:10.1175/1520-0426(1997)014<1298:SDIMSA>2.0.CO;2.

Valenzuela, G., 1967: Depolarization of EM waves by slightly rough surfaces. *IEEE Trans. Antennas Propag.*, **15**, 552–557, doi:10.1109/TAP.1967.1138962.

——, 1978: Theories for the interaction of electromagnetic and oceanic waves—A review. *Bound.-Layer Meteor.*, **13**, 61–85, doi:10.1007/BF00913863.

——, and M. B. Laing, 1970: Study of Doppler spectra of radar sea echo. *J. Geophys. Res.*, **75**, 551–563, doi:10.1029/JC075i003p00551.

Vicen-Bueno, R., C. Lido-Muela, and J. C. Nieto-Borge, 2012: Estimate of significant wave height from non-coherent marine radar images by multilayer perceptrons. *EURASIP J. Adv. Signal Process.*, **2012**, 84, doi:10.1186/1687-6180-2012-84.

——, J. Horstmann, E. Terril, T. de Paolo, and J. Dannenberg, 2013: Real-time ocean wind vector retrieval from marine radar image sequences acquired at grazing angle. *J. Atmos. Oceanic Technol.*, **30**, 127–139, doi:10.1175/JTECH-D-12-00027.1.

Wang, Y., and Y. Zhang, 2011: Investigation on Doppler shift and bandwidth of backscattered echoes from a composite sea surface. *IEEE Trans. Geosci. Remote Sens.*, **49**, 1071–1081, doi:10.1109/TGRS.2010.2070071.

Young, I. R., W. Rosenthal, and F. Ziemer, 1985: A three-dimensional analysis of marine radar images for the determination of ocean wave directionality and surface currents. *J. Geophys. Res.*, **90**, 1049–1059, doi:10.1029/JC090iC01p01049.